



Full Text View

[Volume 32, Issue 9 \(September 2002\)](#)

Journal of Physical Oceanography

Article: pp. 2619–2639 | [Abstract](#) | [PDF \(2.78M\)](#)

Internal Waves and Turbulence in the Upper Central Equatorial Pacific: Lagrangian and Eulerian Observations

R.-C. Lien

Applied Physics Laboratory, University of Washington, Seattle, Washington

E. A. D'Asaro

Applied Physics Laboratory and School of Oceanography, College of Ocean and Fishery Sciences, University of Washington, Seattle, Washington

M. J. McPhaden

National Oceanic and Atmospheric Administration, Pacific Marine Environmental Laboratory, Seattle, Washington

(Manuscript received August 27, 2001, in final form February 25, 2002)

DOI: 10.1175/1520-0485(2002)032<2619:IWATIT>2.0.CO;2

ABSTRACT

In the shear stratified flow below the surface mixed layer in the central equatorial Pacific, energetic near- N (buoyancy frequency) internal waves and turbulence mixing were observed by the combination of a Lagrangian neutrally buoyant float and Eulerian mooring sensors. The turbulence kinetic energy dissipation rate ϵ and the thermal variance diffusion rate χ were inferred from Lagrangian frequency spectral levels of vertical acceleration and thermal change rate, respectively, in the turbulence inertial subrange. Variables exhibiting a nighttime enhancement include the vertical velocity variance (dominated by near- N waves), ϵ , and χ . Observed high levels of turbulence mixing in this low- Ri (Richardson number) layer, the so-called deep-cycle layer, are consistent with previous microstructure measurements. The Lagrangian float encountered a shear instability event. Near- N waves grew exponentially with a 1-h timescale followed by enhanced turbulence kinetic energy and strong dissipation rate. The event supports the scenario that in the deep-cycle layer shear instability may induce growing internal waves that break into turbulence. Superimposed on few large shear-instability events were background westward-propagating near- N waves. The floats' ability to monitor turbulence mixing and internal waves was demonstrated by comparison with previous microstructure measurements and with Eulerian measurements.

Table of Contents:

- [Introduction](#)
- [Experiments and measurements](#)
- [Lagrangian observations](#)
- [Eulerian observations](#)
- [Lagrangian versus Eulerian](#)
- [Discussion](#)
- [Summary](#)
- [REFERENCES](#)
- [FIGURES](#)

Options:

- [Create Reference](#)
- [Email this Article](#)
- [Add to MyArchive](#)
- [Search AMS Glossary](#)

Search CrossRef for:

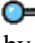
- [Articles Citing This Article](#)

Search Google Scholar for:

- [R.-C. Lien](#)

1. Introduction

The small-scale mixing of momentum and heat is crucial to the dynamics of the equatorial current system and to the large-scale heat budget ([Philander and Pacanowski 1980](#); [McCreary 1981](#); [Crawford and Osborn 1981](#)). In the central equatorial Pacific, the turbulent fluxes of heat and momentum are especially important due to the presence of strong deep-cycle turbulence. The turbulent heat flux across the base of the surface mixed layer is similar in magnitude to the net heat flux across the sea surface ([Gregg et al. 1985](#); [Peters et al. 1988](#); [Moum et al. 1989](#)). The deep-cycle turbulence plays an important role in mediating the heat budget of the surface mixed layer both in the initiation and the termination of the El Niño. A reduction of turbulent heat flux at the base of the mixed layer was found to enhance the increase of the sea surface temperature (SST) during the onset of the 1991–93 El Niño ([Lien et al. 1995](#)). During the termination of the 1998 El Niño, SST dropped precipitously [at some locations by as much as 8°C in a month in the eastern and central equatorial Pacific ([McPhaden 1999](#))]. [Wang and McPhaden \(2001\)](#) suggested that a turbulent heat flux of the order of 100 W m^{-2} was needed to explain the rapid cooling of the SST.

During periods of moderate to strong easterly wind, microstructure measurements in the upper central equatorial Pacific showed intensified turbulence during nighttime extending below the surface mixed layer to about 85-m depth ([Fig. 1](#) ). The nighttime dissipation rate of turbulence kinetic energy (TKE) in the deep-cycle layer exceeded the daytime value by at least a factor of 10. In the deep-cycle layer, the gradient Richardson number (Ri) was close to its critical value, suggesting that shear instability was the potential generation mechanism of the observed strong turbulence. Typical Thorpe and Ozmidov scales of the deep-cycle turbulence were 1–2 m. Occasionally, overturning scales >10 m were observed during energetic mixing events.

Similarly, internal wave activity also intensified in the deep-cycle layer with a distinct diurnal cycle during steady easterly wind. These waves had a frequency near the buoyancy frequency N ([McPhaden and Peters 1992](#)), a horizontal wavelength of hundreds of meters, and a vertical coherence scale of at least 100 m ([Moum et al. 1992](#)). The decay timescale of these deep-cycle internal waves could be as short as 1 h. The estimated wave momentum flux was comparable in magnitude to the surface wind stress ([Lien et al. 1996](#)).

[Gregg et al. \(1985\)](#) hypothesized that internal waves generated at the base of the nighttime mixed layer propagate down into the deep-cycle layer where the superposition of the shear of internal waves with the mean shear of the Equatorial Undercurrent (EUC) triggers instability that results in the intense turbulent mixing in the deep-cycle layer. [Peters et al. \(1994\)](#) showed that the finescale shear of waves intensified at night, supporting Gregg's hypothesis. These waves may be generated as a result of relative motion between the mean flow and “corrugations” of the bottom of the surface mixed layer ([Wijesekera and Dillon 1991](#)), or via shear instabilities within the surface mixed layer ([Skylingstad and Denbo 1994](#)), or as a perturbation of eddies at the base of the convective mixed layer ([Bell 1978](#)).

Alternatively, [Moum et al. \(1990\)](#), [Sun et al. \(1998\)](#), and [Mack and Hebert \(1997\)](#) suggested that shear instability caused the enhancement of internal waves and turbulence in the deep-cycle layer. Shear instability is sensitive to the vertical profile of the mean shear near the base of the surface mixed layer, which has not been adequately resolved in time and space by previous measurements ([Mack and Hebert 1997](#)). Therefore, it is difficult to make direct comparisons between observations and results of linear stability analysis. [Wang et al. \(1998\)](#), using a three-dimensional large eddy simulation (LES) model, qualitatively reproduced the observed deep-cycle turbulence. The Ri of the model results exhibits a diurnal cycle suggesting that the deep-cycle turbulence is closely related to the local shear instability. Recently, [Wang and Müller \(2001\)](#) extended the model domain of [Wang et al. \(1998\)](#) to allow turbulence and internal waves with wavelength of a few hundred meters being adequately resolved. They showed that turbulence and internal waves are generated by the mean shear instability and trigger local instability in the marginally stable deep-cycle layer. [Clayson and Kantha \(1999\)](#) argued that the energetic turbulence and internal waves in the deep-cycle layer result simply from the instability of the background vertical shear of the EUC enhanced by the easterly wind. In their model, nighttime convection eddies in the surface mixed layer and the radiation of internal waves from the base of the mixed layer are not needed to explain the nighttime enhancement of ϵ in the deep-cycle layer.

Differences among these proposed generation mechanisms of internal waves and turbulence are subtle. There is little doubt that the strong vertical shear, primarily associated with the EUC, in the deep-cycle layer causes the shear instability leading to the strong turbulence mixing. Fundamental questions are (i) what triggers the shear instability, internal wave stress, or turbulence stress and (ii) are the observed enhanced internal waves generated by the local shear instability or are they generated remotely, propagating into the deep-cycle layer causing the local shear instability; in either case, there should exist a correlation between intensities of turbulence and internal waves as previously observed. Internal wave potential energy, isotherm displacement, and displacement slope are highly correlated with ϵ in the deep-cycle layer ([Moum et al. 1992](#)). The turbulence energy production rate due to wave stress is significantly correlated with ϵ in the deep-cycle layer ([Lien et al. 1996](#)). Energetic wave packets and strong turbulent mixing were observed at the same time and depth ranges ([Hebert et al. 1992](#)) during two separate intense mixing events. The turbulent dissipation rate increased following a decrease


of internal wave energy, suggesting the wave packet as the energy source of the observed turbulence during the events.

Although a dynamic link between observed high-frequency internal waves and turbulence has been found in statistical properties of previous observations, the correlation between internal wave energy and ϵ break down at smaller time and space scales because internal waves and turbulence have not been observed simultaneously at the same location. It is difficult to associate individual wave breaking and turbulence events in a strong shear regime because the wave propagates while the turbulence is advected by the mean flow. A detailed examination of the wave and turbulence energy budgets will be possible only if turbulence and internal waves are observed simultaneously at the same location.

Here, we describe measurements taken by a Lagrangian float deployed in the deep-cycle layer at the central equatorial Pacific and Eulerian measurements taken at nearby moorings of the Tropical Atmospheric Ocean (TAO) array (McPhaden et al. 1998). The Lagrangian float and its deployment, sensors on the moorings, and the background conditions in the central equatorial Pacific are described in section 2. In sections 3 and 4, we present analysis results of the Lagrangian measurements and Eulerian measurements, respectively. An event of shear instability encountered by the Lagrangian float is shown. The Doppler shift identified by comparing Eulerian and Lagrangian spectra is discussed in section 5. Length scales of near- N internal waves and turbulence, possible generation mechanisms of internal waves, and effects of the deep-cycle turbulent heat flux on the heat budget of the surface mixed layer are discussed in section 6. Results are summarized in section 7.


2. Experiments and measurements


a. Lagrangian float and deployment

Lagrangian measurements were taken by neutrally buoyant deep “Lagrangian floats” (DLF) (Fig. 2 ). These are designed to accurately follow water motions at high frequencies through a combination of a float density that matches that of seawater and a high drag screen. The density of the float is initially matched to that at the target depth using a piston on the float that changes the float's volume (D'Asaro et al. 1996). The float's compressibility closely matches that of seawater so it stays at the same density as seawater despite vertical excursions. The float's volume is adjusted on a timescale of several days to keep its depth near the target depth. The float is therefore “isopycnal” on timescales shorter than a few days and “isobaric” on longer timescales. The float measures temperature along its path with an accuracy of about 10^{-3} °C.

Float deployments in a variety of flows, both wavelike and turbulent, show the float to be approximately Lagrangian (D'Asaro et al. 1996; D'Asaro and Dairiki 1997; Farmer et al. 1997; D'Asaro 2001). The non-Lagrangian behavior is due primarily to the finite size of the float because it cannot accurately follow motions smaller than itself. Lien et al. (1998) analyze this effect for turbulent flows, show that it occurs only at high frequencies, and derive a response function to correct for it.

On 2224 LT 28 September (yearday 270.93) 1998, we deployed two DLFs on the equator at 140°W during routine TAO mooring operations. The equatorial Pacific was in a La Niña phase and the central equatorial Pacific was $\sim 2^\circ\text{C}$ colder than normal. On the basis of real-time data from TAO buoys, two DLFs were targeted at isopycnal surfaces at 45-m and 55-m depths. Unfortunately, the DLF deployed at 55-m depth failed for an unknown reason. The DLF deployed at 45-m depth successfully took 8-days of measurements. It sampled every 300 s in the first half-day while measuring the vertical profile of temperature and ballasting the float. In the following 4 days (yearday 271.43–275.43), the float sampled every 30 s to resolve both internal waves and turbulence. It then switched to a 300-s sampling rate in the last 3.5 days (yearday 275.43–278.93). The low sampling rate was chosen to reduce the data transmission time through Argos. Before it surfaced to transmit data via Argos, the DLF profiled from 90-m to 10-m depths measuring the vertical structure of temperature. Our analysis focuses only on the 4-day high-sampling-rate data between yeardays 271.43 and 275.43 because measurements in other periods, with 300-s sampling interval, did not adequately resolve internal waves and missed the turbulence inertial subrange completely.

A CTD profile was taken immediately before deployment of the DLFs and velocity measurements were taken continuously by the ship-mounted 150-kHz narrowband ADCP on board *Ka'imimoana*. The vertical profile of temperature observed by the float during its descent agreed well with temperature taken by the CTD (Fig. 2 ). The float fluctuated between depths 30 and 60 m during the experiment. The EUC had its maximum speed of 1.3 m s^{-1} at 90-m depth. The meridional current was southward with a uniform speed -0.5 m s^{-1} between depth 30 and 60 m, a signature of tropical instability waves. The meridional component of vertical shear was much smaller than the zonal component. At 45-m depth, the buoyancy frequency was 0.013 s^{-1} (hereafter referred to as N_{CTD}), and the vertical shear of the mean zonal flow was 0.03 s^{-1} . This resulted in a Richardson number Ri of 0.19, indicating a favourable condition for shear instability.

Time series of Lagrangian measurements of pressure and temperature, estimates of vertical velocity, and the rms vertical velocity during the 4-day high-sampling-rate period of the experiment are shown in Fig. 3 , together with the easterly

wind speed measured on the TAO buoy and the vertical shear of the zonal velocity computed by current-meter measurements at depths 10 and 25 m. The vertical velocity is obtained by the time derivative of the measured pressure. These time series will be discussed in [section 3](#).

b. Eulerian observations on the mooring

To complement the study of the deep-cycle layer, we deployed five fast-response Mini Temperature Recorders (MTRs) with 10-s response time at depths 25, 35, 45, 55, and 70 m on the 0°, 140°W TAO moorings. The MTRs sampled every 20 s for 13 days following the deployment of DLFs. There were 11 standard temperature sensors mounted at depths of 5, 10, 25, 45, 60, 90, 100, 120, 140, 200, and 500 m on the moorings. Temperature measurements taken between yeardays 271.5 and 284 are shown in [Fig. 4](#). Vector Averaging Current Meters and Vector Measuring Current Meters were attached to the moorings line at five depths in the upper 120 m. Surface wind was measured by an R.M. Young sensor mounted 4 m above mean sea level on the buoy. A 150-kHz upward-looking narrowband ADCP was suspended at 285-m depth on the mooring providing horizontal velocity measurements at 5-m vertical intervals below 30 m.

c. Background conditions

During the float experiment, the equatorial Pacific was in a La Niña phase subsequent to the 1997–98 El Niño ([McPhaden 1999](#)). Between May and June 1998 the air temperature and SST at equator 140°W decreased from 28° to ~22°C in 4 weeks, signaling the termination of the El Niño ([Fig. 5](#)). The surface wind was easterly varying between 2 and 7 m s⁻¹, the EUC exceeded 1 m s⁻¹ shoaling from depth 80 to 60 m, and the meridional current was generally <0.2 m s⁻¹ in the upper 250 m. After July 1998, the surface wind increased gradually, the EUC weakened and deepened, and the meridional velocity showed vertically coherent bands with a period of ~1 month associated with tropical instability waves.

During the float experiment, the easterly wind was stronger than it had been since the beginning of 1998, resulting in a strong shear in the upper water column. The core of EUC was at about 90-m depth and tropical instability waves were well developed with a magnitude about 0.5 m s⁻¹. The speed of the south equatorial current (SEC) in the upper 50 m was greater than 0.5 m s⁻¹. Fortunately, the float was deployed within the strong mean shear below the surface mixed layer. Before and after the float observation period, the vertical shear of the zonal velocity was weak, suggesting weaker shear instability and deep-cycle turbulence.

Details of the surface wind, the shear, the stratification, $Ri (=N^2/S^2)$, and the reduced shear squared (S^2-4N^2) are shown in [Fig. 6](#) for a 13-day period encompassing the float and the MTR experiments. The hourly average wind fluctuated between 6 and 10 m s⁻¹ in the first 4 days, gradually decreased to <4 m s⁻¹, and then increased to 6–7 m s⁻¹. The vertical shear squared in the upper 80 m was stronger than 10⁻³ s⁻² in the first 3 days and decreased afterward. Although the reduction of shear was accompanied by the reduction of stratification, the condition for shear instability ($Ri < 1/4$ and positive reduced shear squared) did not persist. Background conditions in yeardays 275 and 277–280 were unfavorable for shear instability. The reduced shear squared was the strongest in the first 3 days and decreased one day before the wind decreased suggesting that the vertical shear was subject to large-scale processes.

3. Lagrangian observations in the deep-cycle layer

The depth of the DLF fluctuated between depth 30 and 60 m and was always below the surface mixed layer, which was shallower than 25 m ([Fig. 3](#)). Temperatures at depths 5 and 10 m were nearly identical and were ~1°C warmer than at 25-m depth ([Fig. 4](#)). The wind was easterly with a speed of 6–9 m s⁻¹. The vertical shear of zonal velocity measured by current meters mounted at depths of 10 and 25 m on the mooring varied between -0.06 and -0.11 s⁻¹ representing the vertical shear across the base of the surface mixed layer ([Fig. 3a](#)). This vertical shear exhibits a hint of diurnal variation. It was the strongest each day immediately before the sunset, for example, days 0.75, 1.75, and 2.75, and the weakest each day around local noon, for example, days 1.5 and 2.5. The diurnal variation of the shear across the base of the surface mixed layer was primarily due to fluctuations of the zonal current below the surface mixed layer.

The vertical velocity of the DLF is estimated as the time rate of change of the float depth. The variance of vertical velocity showed a clear enhancement at nighttime with an rms value of 0.01 m s⁻¹ at daytime increasing to >0.015 m s⁻¹ at nighttime ([Fig. 3](#)). Most of the vertical velocity variance resided in a frequency band slightly below local N (shown later). During the 4-day experiment of float observations, a buoyancy frequency N_{dlf} of 0.015 s⁻¹ in the depth range of 30–65 m is a good approximation ([Fig. 4c](#)). Temperature fluctuations recorded on the float varied between 19° and 22°C and were much smoother than measurements taken from the mooring, which showed ±0.4°C high-frequency fluctuations that resulted from the vertical advection by near- N internal waves ([Figs. 3e](#) and [4d](#)). For a perfect Lagrangian float, temperature can only change by the turbulence mixing.

a. Theoretical Lagrangian spectrum

Both internal waves and turbulence exist in the stratified flow and it is often difficult to separate them. [D'Asaro and Lien \(2000\)](#) demonstrated that these two motions can be separated by the Lagrangian frequency observed in Lagrangian measurements. Internal waves exist at $\omega \leq N$ and turbulence exists at $\omega > N$. This is entirely consistent with linear internal wave dynamics and with Ozmidov scaling such that turbulence exists at scales smaller than the Ozmidov length scale $L_O = \epsilon^{1/2} N^{-3/2}$ and internal waves exist at larger scales.

In an energetic stratified turbulent flow, Lagrangian frequency spectra of vertical velocity $\Phi_w(\omega)$ have a universal spectral form, white below N and ω^{-2} beyond N ([D'Asaro and Lien 2000](#)). Accordingly, vertical acceleration spectra $\Phi_a(\omega)$ are ω^2 at $\omega < N$ and white at $\omega > N$, which is the turbulence frequency inertial subrange. In the inertial subrange, the spectral level of $\Phi_a(\omega)$ is linearly proportional to ϵ ; that is, $\Phi_a = \beta\epsilon$, where $\beta = 1.8$ is a universal Kolmogorov constant ([Lien et al. 1998](#); [Yeung 2001](#)). Because of the finite size of the float, observed Lagrangian frequency spectra are attenuated at $\omega \geq \epsilon^{1/3} L^{-2/3}$, where L is the scale of the float ([Lien et al. 1998](#)).

In homogeneous turbulent flow, the Lagrangian frequency velocity and acceleration spectra exhibit the same universal spectral forms as in the stratified turbulent flows with the buoyancy frequency N replaced by the overturning frequency of large eddies. In the surface mixed layer, the large-eddy frequency is scaled as $\sigma_w H^{-1}$, where σ_w is the vertical velocity scale and H is the thickness of the surface mixed layer. The universal form of Lagrangian frequency velocity spectra in the turbulence inertial subrange has also been suggested by the dimensional analysis ([Tennekes and Lumley 1972](#)), but with a smaller β of 1.2. The value of β depends on the turbulent energy distribution in wavenumber-frequency space. Observed Lagrangian frequency spectra of vertical velocity and acceleration in the surface mixed layer suggest $\beta = 1.8$ ([Lien et al. 1998](#)).

On the basis of the dimensional analysis, in the turbulence inertial subrange the Lagrangian frequency spectrum of the time rate of change of temperature $\Phi_{d_t\theta}(\omega)$ should scale as the diffusion rate of temperature variance χ ([Yeung 2001](#)). The scaling factor could be derived following the analysis by [Lien et al. \(1998\)](#) or [Tennekes and Lumley's \(1972\)](#) procedure for deriving the acceleration Lagrangian frequency spectrum. We will briefly describe these approaches.

In the turbulence inertial subrange, the wavenumber spectrum of temperature has a universal form $\Phi_\theta(k) = \alpha_\theta \chi \epsilon^{-1/3} k^{-5/3}$, where k is the wavenumber magnitude, and $\alpha_\theta = 0.5$ is the Kolmogorov constant for the temperature spectrum ([Williams and Paulson 1977](#); [Dillon and Caldwell 1980](#)). [Tennekes and Lumley \(1972\)](#) assumed a relation between the Lagrangian frequency and wavenumber as $\omega = \epsilon^{1/3} k^{2/3}$ so that turbulence evolves on its advection timescale. Eddies at a scale of k^{-1} have a unique frequency ω for a given ϵ , that is, zero spreading. The Lagrangian frequency spectrum and wavenumber spectrum is related as $\Phi_\theta(k)dk = \Phi_\theta(\omega)d\omega$ by preserving temperature variance in any wavenumber band and the corresponding frequency band. Consequently, we can derive an expression for the Lagrangian frequency spectrum of temperature as $\Phi_\theta(\omega) = \beta_\theta \chi \omega^{-2}$, where $\beta_\theta = 0.75$ is a universal constant.

[Fung et al. \(1992\)](#) suggest a Gaussian spreading function in which eddies at a scale of k^{-1} spread its energy at frequencies in a Gaussian form centering at frequency $\epsilon^{1/3} k^{2/3}$ with a frequency bandwidth of $\epsilon^{1/3} k^{2/3}$. With the Gaussian spreading, we find the same expression for $\Phi_\theta(\omega)$ with the Kolmogorov constant $\beta_\theta = 1.13$. In the following analysis, we will use $\beta_\theta = 1.13$ because previously observed vertical acceleration spectra were explained better by the model spectrum derived by assuming a Gaussian spreading.

Therefore, we expect that in the turbulence inertial subrange the Lagrangian frequency spectrum of the time rate of change of temperature should have a universal form as $\Phi_{d_t\theta}(\omega) = \beta_\theta \chi$. The diffusion rate of the temperature variance χ could be inferred directly from the spectral level of $\Phi_{d_t\theta}$ in the inertial subrange.

In the turbulence inertial subrange, the wavenumber spectrum of temperature $\Phi_\theta(k)$ depends on both ϵ and χ , whereas the Lagrangian frequency spectrum $\Phi_\theta(\omega)$ depends on χ only. This fundamental difference is due to the fact that temperature is a passive scalar advected by the turbulence. The $\Phi_\theta(k)$ measures temperature fluctuations not only due to the mixing, related to χ , but also due to the turbulence advection, scaled by ϵ . The Lagrangian frequency spectrum $\Phi_\theta(\omega)$,

however, does not measure temperature fluctuations advected by the direct estimate of χ . In fact, in the inertial subrange the Lagrangian frequency spectrum of any passive tracer should scale by its diffusion rate only, independent of ϵ .

b. Observed Lagrangian spectra

To reveal the diurnal variation of internal waves and turbulence, we computed Lagrangian spectra of vertical velocity Φ_w , vertical acceleration Φ_a , and the time rate of change of temperature $\Phi_{d\theta}$ in four different time periods of the day; 1200–1800 LT (afternoon), 1800–2400 LT (evening), 2400–0600 LT (night), and 0600–1200 LT (morning) (Fig. 7). Except for the fourth day, Φ_w , Φ_a , and $\Phi_{d\theta}$ all exhibited a significant nighttime enhancement at $\omega \geq N_{\text{diff}}$. The specific time of day when spectra reached their maximum varied, for example, evening in the first day, night in the second, and third days. At $\omega \ll N$, spectra did not show significant diurnal variation.

Vertical velocity spectra exhibited a distinct peak slightly below N (Figs. 7a–d and Fig. 18). This spectral peak was often >10 times the background spectral level.

Desaubies (1973) demonstrated analytically that observed spectral peak of velocity and temperature frequency spectra near the local buoyancy could be explained by the turning point effect of internal waves. The magnitude of spectral peaks vary with the vertical gradient of background buoyancy frequency and the low wavenumber bandwidth of the internal waves. The accumulated energy near the local N is due to the leakage of low-mode energy at adjacent depths with greater N .

We suggest that our observed near- N spectral peak is not due to the effect of the turning point (Desaubies 1973) because (i) observed near- N waves were sometimes in the depth region of constant N without vertical gradient, (ii) the spectral magnitude of observed near- N waves relative to the background waves was much greater than to be expected by the effect of the turning point, and (iii) vertical velocity spectra estimated from the mooring temperature measurements have the spectral peak at the same frequency (Eulerian frequency) even when N varies in depths. Instead, we believe that the observed near- N internal waves are results of shear instability in the deep-cycle layer.

Vertical acceleration spectra show a spectral plateau in the inertial subrange. The spectral roll-off near the Nyquist frequency (0.1 s^{-1}) is due to the spline-fitting effect in computing the acceleration from the vertical velocity. Because of the time differencing effect, the temporal resolution of the vertical acceleration is about 60 s. This yields a resolvable turbulence inertial subrange $\omega \geq N_{\text{diff}}$ less than one-half a decade of the frequency domain. Nevertheless, the diurnal variation of the vertical acceleration spectrum in the turbulence inertial subrange is discernible. The float has an overall pressure noise of ~ 0.002 db. The white pressure noise introduces an ω^4 spectral slope in the vertical acceleration spectrum and emerges from observed spectra at high frequencies when turbulence is weak (Fig. 8). At low frequencies and when turbulence is strong, the pressure noise does not affect the estimate of ϵ . The lower bound of estimate of ϵ is slightly below $5 \times 10^{-8} \text{ W kg}^{-1}$.

Spectra of the thermal change rate were white in nearly the entire frequency range during daytime and nighttime. The roll-off at $\omega \geq 0.08 \text{ s}^{-1}$ is again due to the time differencing effect. There is no signature of the buoyancy frequency on spectra. A hint of change of spectral slopes exists in some spectra at 0.005 s^{-1} , roughly at the peak of the vertical velocity spectrum. Within the inertial subrange, $\omega \geq N_{\text{diff}}$, the diurnal variation of spectral levels corresponds very well with that of vertical acceleration spectra. The spectral level of thermal change rate in the inertial subrange provides estimates of χ . Spectral levels of vertical acceleration and thermal change rate in the inertial subrange showed a factor of 20 decrease during the 4-day period.

c. General turbulence properties and diurnal cycle

Lagrangian frequency spectra of vertical acceleration and thermal change rate computed in hourly segments were used to estimate ϵ and χ , respectively, based on the spectral levels in the turbulence inertial subrange. The response function due to the finite-size effect of the float has been applied to vertical acceleration spectra. Estimates of ϵ varied between 10^{-8} and $10^{-5} \text{ W kg}^{-1}$ (Fig. 9). Fitting a linear trend to $\log_{10}(\epsilon)$ showed a factor of 20 decrease in 4 days. Bursts of strong ϵ occur in the night and were often 100 times the background level. After removing the linear trend, the nighttime increase of ϵ could be identified slightly easier in the first 3 days. We computed the eddy viscosity, $K_m = \epsilon S^{-2}$, using the dissipation method assuming a local balance between ϵ and shear production, where $S^2 = (\partial_z u)^2 + (\partial_z v)^2$ is the total shear squared. Hourly averages of total shear squared S^2 were computed using ADCP velocity measurements taken on the TAO mooring.

The eddy diffusivity is computed as $K_p = 0.2\epsilon N^{-2}$ (Osborn 1980). It agrees well with K_m as found by previous microstructure experiments (e.g., Peters et al. 1988). This corresponds to a nearly constant Ri ($=N^2 S^{-2}$) in the deep-cycle layer. The Ri tends to stay at the level of 0.25, critical to the shear instability. Wang et al. (1998) found a similar low-Ri layer in their LES model of the deep-cycle layer. Temperature measurements between depths 30 and 60 m taken by the sensors mounted on the TAO mooring were hourly averaged and were used to compute the hourly averaged N assuming a constant salinity of 34.75 psu. The CTD profile taken before the deployment of the float showed salinity increase from 34.6 to 34.9 psu with depths between 30 and 60 m. During the course of the first 4 days of the experiment, N varied by less than a factor of 2 in depths between 30 and 70 m (Fig. 4).

We constructed a composite-day variation of ϵ using detrended estimates of ϵ (Fig. 9d). The composite ϵ showed an increase after the sunset ($h = -6$) and a decrease after the sunrise ($h = 6$). The hour-by-hour variation of ϵ was sometimes greater than the night-to-day variation. A large value of ϵ also existed at hour 10, which resulted primarily from a single observation at day 1.4 (Fig. 9a). Our composite-day variation of ϵ agreed with that of Tropical Instability Wave Experiment (TIWE) observations, although our observations exhibited greater hour-by-hour fluctuations presumably due to a smaller number of observations. The composite day of TIWE showed a gentle increase of ϵ after sunset and a gentle decrease about 3 h after the sunrise. Caldwell et al. (1997) proposed that the remnant shear production in the deep-cycle layer supports strong ϵ several hours after the sunrise. The ϵ at nighttime was about a factor of 10 greater than ϵ at daytime for both the present and TIWE observations.

Time series of χ also showed a linear decrease of $\log_{10}(\chi)$ (Fig. 10). After removing the linear trend, the nighttime increase of χ was easier to identify, even at the fourth day (Fig. 10d). The diurnal variation of ϵ in the fourth day was invisible in our observations presumably due to the contamination by the pressure noise on the estimate of ϵ . The thermal diffusivity computed as $K_h = 0.5\chi(d\bar{\theta}/dz)^{-2}$ (Osborn and Cox 1972) agreed with K_p most of the time, as found in the previous experiment (e.g., Peters et al. 1988). On the fourth day, K_p exceeded K_h reflecting, again, the overestimate of ϵ contaminated by the pressure noise.


The heat flux was computed as $J_q = \rho C_p K_h \partial_z \bar{\theta}$, where C_p is the heat capacity ($\sim 4000 \text{ J K}^{-1} \text{ kg}^{-1}$). This represents a general magnitude of turbulence heat flux in the deep-cycle layer. Because the large-scale temperature gradient $\partial_z \bar{\theta}$ did not vary greatly during our observational period, the variation of estimated J_q reflects primarily the change of K_h . The turbulence heat flux varied between $O(1) \text{ W m}^{-2}$ to $O(10^3) \text{ W m}^{-2}$ in this 4-day period. Our estimates of J_q in the first two days exceeded those obtained from previous microstructure measurements during the Tropic Heat Experiment and TIWE, $\sim 50 \text{ W m}^{-2}$. Our observations in the first two nights, $\epsilon > 5 \times 10^{-6} \text{ W kg}^{-1}$, represent periods of extremely strong turbulence mixing. Estimates of ϵ , χ , and J_q on the third day were closer to the averages of previous microstructure observations.

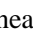
The agreement between K_p and K_h is shown in Fig. 11. We have excluded estimates of the last day when our estimates of ϵ were significantly contaminated by instrument noise. Our result provides a mutual consistency check of our estimates of ϵ and χ from float spectra.

d. A shear instability event

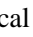
Some previous studies have suggested that observed internal waves in the deep-cycle layer are generated via shear instability processes (e.g., Moum et al. 1992; Mack and Hebert 1997; Sun et al. 1998; Clayson and Kantha 1999). Observed internal waves have a near- N frequency and a horizontal wavelength of few hundred meters. Events of shear instability within the deep-cycle layer have been identified by Hebert et al. (1992). These previous observations were taken from towed thermistor chains and revealed the spatial structure of the instability billows. Here, we present further evidence of shear instability recorded by the Lagrangian float. Because the float is advected by the current, its measurements should provide the information of the dynamical evolution of the instability billow. Two bursts of strong ϵ and χ were found in the first night (29 September) of float measurements (Figs. 9 and 10). Here, we discuss in detail the first burst.


Between 1900 and 2030 LT 29 September, the vertical velocity showed clear narrowband fluctuations at frequencies slightly below N with increasing amplitudes (Fig. 12b). The float moved vertically between 35 and 53 m (Fig. 12a) and the temperature remained nearly constant except between 2030 and 2230 LT when large temperature fluctuations occurred (Fig. 12d). The frequency of the dominant vertical velocity variance can be identified more easily from the wavelet analysis (Fig. 13). We performed a wavelet analysis on observations of vertical velocity (Percival and Guttorp 1994). Wavelet spectral density $\Phi_w(\omega)$ were calculated by dividing wavelet variances by the corresponding frequency bands at each time. Between 2030 and 2120 LT, these energetic narrowband fluctuations burst into higher-frequency broadband disturbances, decaying after 2120 LT, and were almost indiscernible after 2200 LT.

We interpret this event as 1) near- N internal waves generated by the shear instability between 1900 and 2030 LT, 2) turbulence generated by breaking internal waves between 2030 and 2120 LT, and 3) turbulence dissipated after 2120 LT. The evolution of vertical velocity variance in time–frequency space during this event is shown in [Fig. 13b](#) . A transition period was observed when the frequency content of the vertical velocity variance shifted from $\sim 0.01 \text{ s}^{-1}$ to higher frequencies between 1900 and 2100 LT. Before 2030 LT, vertical velocity variance was at frequencies below N . Between 2030 and 2200 LT, strong vertical velocity variances were found in the turbulence inertial subrange, $\omega > N$.


The time evolution of vertical velocity variances at various frequency bands extracted from the wavelet analysis was examined. The resolved wavelet frequencies of interest were 0.1047, 0.0524, 0.0262, 0.0131, and 0.0065 s^{-1} with the corresponding four frequency bands centering at 0.0785, 0.0393, 0.0196, and 0.0098 s^{-1} . The first three frequency bands were in turbulence inertial subrange, and the fourth frequency band encompassed the near- N frequency band of internal waves. The vertical velocity variance in the near- N frequency band (gray curve in [Fig. 13](#) ) , $0.0065 \text{ s}^{-1} < \omega < 0.0131 \text{ s}^{-1}$, showed a gentle increase between 1900 and 2030 LT with an exponential growing timescale of $\sim 1 \text{ h}$, and was saturated at 2030 LT for 1/2 h before it decayed at 2100 LT. The vertical velocity variance in the inertial subrange, $\omega > 0.0131 \text{ s}^{-1}$, grew at 2030 LT when internal wave energy saturated. The exponential growing and decaying timescale of the vertical velocity variance in the inertial subrange during this period was $\sim 10 \text{ min}$, ~ 1 buoyancy period. The increase of vertical velocity variance in the inertial subrange exceeded the vertical velocity variance of internal waves suggesting the mean shear contribution to the turbulence.

The estimated 1-h exponential growth timescale of internal waves is consistent with the results of linear stability analysis by [Sun et al. \(1998\)](#) on the basis of the background conditions during TIWE. They find the mode-1 waves, generated at the critical level within the SEC, have an exponential timescale varying between 30 and 73 min, strongly sensitive to the background shear and stratification. The mode-1 wave has a westward phase velocity identical to the velocity of the SEC at the critical level where the Ri is also subcritical. The Eulerian frequency of the mode-1 wave is about 0.006 s^{-1} . The fastest growing mode in the analysis of [Sun et al. \(1998\)](#) is the mode-2 waves, which have the critical level at the boundary between the SEC and EUC. The mode-2 wave is nearly stationary and shows a vertical phase shift across the critical level. Temperature measurements taken by the TAO mooring at various depths do not exhibit any phase shift across the boundary between SEC and EUC, around 45 m between days 271 and 274. Therefore, the mode-2 wave does not seem to exist in our observations. [Mack and Hebert \(1997\)](#) perform a similar linear stability analysis using the background condition of the Tropic Heat 2 experiment during April of 1987. They find that the mode-1 waves have an e -folding growth time of less than 10 min, much faster than that found by [Sun et al. \(1998\)](#). Their solutions are highly sensitive to the assumed velocity structure in the uppermost 40 m.

We computed turbulent fluctuations of vertical velocity and temperature by high-pass filtering float measurements at frequencies greater than 0.01 s^{-1} ([Fig. 12](#) ). Turbulent fluctuations of vertical velocity and temperature enhanced between 2030 and 2200 LT. Before and after this turbulent period, vertical velocity and temperature were dominated by internal waves at frequencies smaller than 0.01 s^{-1} . The heat flux J_q was computed as $-\rho C_p \langle w' \theta' \rangle$. During the event, the heat flux reached $>4000 \text{ W m}^{-2}$. The average heat flux between 2030 and 2200 LT was 830 W m^{-2} , consistent with our estimate based on the thermal diffusivity and large-scale temperature gradient. Before and after the event, the heat flux varied between $\pm 50 \text{ W m}^{-2}$, averaged to zero. Our estimated heat flux during this event was at least an order of magnitude greater than previous estimates by microstructure observations.

The float is nearly Lagrangian and should stay on the isopycnal surface if there is no turbulence mixing. At the float observational site, the T - S relation was tight and the isothermal surface was an appropriate surrogate for isopycnal surface. Despite the $\sim 10 \text{ m}$ vertical displacement of the float, the temperature remained nearly constant before and after the turbulent event because there was no strong diapycnal mixing ([Fig. 14](#) ). During the event between 2030 and 2200 LT, the float encounters large temperature changes showing three clockwise loops in θ - Z phase spaces, one at 45–47 m and 21° – 21.6°C (centering at 2040 LT), one at 48–52 m and 20.6° – 21.2°C (centering at 2100 LT), and one at 34–42 m and 21.2° – 21.8°C (centering at 2120 LT). The average heat flux along the float's trajectory can be computed as ([D'Asaro et al. 1996](#))

$$J_q = -\rho C_p \int \theta' w dt = -\rho C_p \oint \theta' dz. \quad (1)$$

A counterclockwise loop in the θ' – Z space represents a typical convection, that is, cold (warm) water downward (upward). The clockwise loop represents a mixing process such that warm (cold) water moves downward (upward). The corresponding heat flux for these three mixing events are 1, 5, and 0.5 kW m^{-2} ([Fig. 12f](#) ).

Our estimates of the heat flux (Figs. 12f and 14) are sensitive to the assumed large-eddy frequency cutoff of turbulence because temperature has a red spectrum. The cospectrum and quadspectrum between temperature and vertical velocity, computed using measurements between 2030 and 2130 LT, have a similar magnitude in the entire frequency range (Fig. 15). The cospectrum, representing the heat flux, is dominantly negative. We computed the integrated heat flux as

$$J_Q(\omega) = \int_{\omega_{Nq}}^{\omega} \rho C_p C_{\omega\theta} d\omega. \quad (2)$$

The J_Q increased gradually in the frequency band between 0.06 and 0.015 s^{-1} reaching 1500 $W m^{-2}$ at 0.015 s^{-1} , dropped slightly between 0.015 s^{-1} and 0.01 s^{-1} , and increased sharply at $\omega < 0.008 s^{-1}$. Our estimates of heat fluxes (Figs. 12f and 14) do not include effects at $\omega < 0.01 s^{-1}$, which we assume as due to internal waves.

Spectra of vertical acceleration and the thermal change rate showed significant increase during the turbulent event (Fig. 16). Spectra computed using measurements taken before and after the event were nearly identical. During the event, between 2030 and 2130 LT, ϵ was $2 \times 10^{-5} W kg^{-1}$, and χ was $10^{-4} \text{ }^\circ C^2 s^{-1}$. Hebert et al. (1992) reported a similar magnitude of ϵ in an overturning event in the deep-cycle layer. The eddy diffusivity and thermal diffusivity estimated from ϵ and χ in the event was 0.012 and 0.007 $m^2 s^{-1}$, respectively, and the heat flux was $\sim 4000 W m^{-2}$.

4. Eulerian observations

Five mini temperature recorders were mounted on the TAO mooring at depths 25, 35, 45, 55, and 70 m. The MTR had a 10-s response time and was set to measure temperature at 20-s sampling intervals aimed at resolving internal waves (Fig. 4). These measurements were taken for a 13-day period beginning 29 September 1998. The first 8 days of measurements overlapped with float observations. There were also standard temperature sensors mounted on the TAO mooring at depths 5, 10, 25, 45, 60, 80, 100, 120, 140, 200, and 500 m taking temperature measurements every hour. Before day 276, the mixed layer was shallower than 25 m, and the vertical gradient of temperature remained nearly constant between 25 and 60 m. The base of the surface mixed layer reached at least 25 m at day 276.

We compute spectra of temperature averaged between depths 25 and 55 m in 6-h intervals, designated as morning, afternoon, evening, and night, following the same procedure as for the spectral analysis of float measurements (Fig. 17). Only spectra in the first 12 days are shown. Cross-spectral analysis of measurements at different depths indicates that temperature fluctuations between 25 and 55 m are strongly coherent and in phase in the internal wave frequency band (not shown). The incoherent component exists in the turbulence frequency band. Therefore, the vertical averaging does not alter spectral properties of temperature in the internal wave frequency band.

During the first day, spectra peaked at $\omega \approx 0.01 s^{-1}$, a near- N frequency, at nighttime and the next morning. This is the same night the float encountered the instability billow discussed in the previous section. On days 2–4, spectra showed significant difference among four 6-h time periods, especially at frequencies greater than 0.01 s^{-1} . This pattern disappeared on days 5–8, but occurred again on days 9–12. The specific time when the temperature spectrum at frequencies greater than 0.01 s^{-1} had the highest spectral level varied day to day without a clear pattern.

In the internal wave frequency band, we expect an ω^{-2} spectral slope for temperature spectra (Garrett and Munk 1975). Our observed spectra at $\omega \ll 0.01 s^{-1}$ had spectral slopes consistent with ω^{-2} , although sometimes spectral slopes at low frequencies were obscured by the spectral bump near N . In the turbulence inertial subrange, the temperature wavenumber spectrum has a spectral slope of $k^{-5/3}$, where k is the wavenumber. If the high-frequency variation of temperature observed on the mooring was due to the turbulent temperature spatial structure advected by the mean flow, a frequency spectral slope of $\omega^{-5/3}$ is expected for $\omega > Uk_0$, where U is the mean velocity and k_0 is the length scale of large eddies. In the deep-cycle layer, the Ozmidov scale is about 1 m (Lien et al. 1995), which is generally believed to be the vertical scale of large eddies. Assuming isotropic turbulence, k_0 is $\sim 1 m^{-1}$. The zonal velocity in the EUC is a strong function of depth and the meridional velocity dominated by the tropical instability waves during this period is vertically coherent with a maximum velocity magnitude of 0.5 $m s^{-1}$. The spectral slope at frequencies greater than 0.01 s^{-1} sometimes showed a clear $-5/3$ slope, for example, days 1, 4, 11, and 12, but it often was hard to distinguish between -2 and $-5/3$ slopes. Therefore, we could not conclude whether the observed significant diurnal variation of temperature spectra at high frequencies was due to advected turbulence or internal waves.

5. Lagrangian versus Eulerian measurements

Here, we compare Lagrangian and Eulerian frequency spectra of vertical velocity and extract properties from their difference. The Lagrangian float provides direct measurements of vertical velocity. To obtain estimates of vertical velocity from Eulerian measurements, the linear internal wave dynamics has to be assumed (Müller et al. 1978) such that

$$\hat{w} = -\partial_t(\theta - \bar{\theta})/\partial_z\bar{\theta}, \quad (3)$$

where $\bar{\theta}$ is the daily average temperature. Lagrangian and Eulerian frequency spectra computed during the first 4 days were compared (Figs. 18c–f). In general, the two spectra are indistinguishable at frequencies below 0.01 s^{-1} suggesting the linear internal waves assumption (3) is appropriate at low frequencies. Lagrangian and Eulerian measurements show a similar weak diurnal variation of vertical velocity variances integrated at frequencies below 0.01 s^{-1} (Fig. 18b).

During the first 3 days, the near- N spectral peak also appears at the same frequency and similar spectral levels. In the fourth day, however, the near- N spectral peak is at frequency of 0.01 s^{-1} for the Eulerian spectrum and at 0.0065 s^{-1} for the Lagrangian spectrum. The difference between the Lagrangian frequency (intrinsic frequency) ω and Eulerian frequency (encounter frequency) σ is the Doppler shift; that is,

$$\omega = \sigma - \mathbf{U} \cdot \mathbf{k}, \quad (4)$$

where \mathbf{U} is the mean velocity vector, and \mathbf{k} is the wavenumber vector. When the component of mean current parallel to the wave vector vanishes, the intrinsic frequency is identical to the encounter frequency. This appears to be the case for the first three days when the mean zonal current at 45-m depth was nearly zero. Previous observations suggest internal waves in the deep-cycle layer propagate dominantly in the east–west direction. Therefore, in the first 3 days the Doppler shift frequency is zero. On the fourth day, the mean zonal current changed from zero to -0.3 m s^{-1} with a mean of -0.2 m s^{-1} . Assuming that waves propagate predominantly in the zonal direction, the difference between the Eulerian and Lagrangian frequencies implies that near- N waves propagate westward with a zonal wavelength of $\sim 360 \text{ m}$ and a phase speed of 0.5 m s^{-1} . If we further assume the WKB approximation and apply the dispersion relation of linear internal waves, the vertical phase speed is found to be 0.27 m s^{-1} . The vertical energy speed is -0.22 m s^{-1} and the westward energy speed is -0.47 m s^{-1} . If these near- N waves resulted from the shear instability, the estimated zonal phase velocity of -0.5 m s^{-1} implies that the shear instability occurs at a depth shallower than 35 m where the mean zonal current matches the wave phase velocity (not shown).

6. Discussion

a. Length scales

Lagrangian float measurements also provide estimates of length scales of near- N internal waves and turbulence. The Ozmidov scale, $L_O = \epsilon^{1/2} N^{-3/2}$, is the turbulence large-eddy length scale at which the inertial force balances with the buoyancy force. The length scale, $L_w = \sigma_w N^{-1}$, represents the vertical scale of near- N waves. Estimates of length scales are shown in Fig. 19. As expected, the internal wave length scale L_w is generally greater than the large-eddy length scale L_O . Exceptions occur during events of strong shear instability when ϵ is extremely strong and the large-eddy length scale becomes compatible with the length scale of near- N waves. The compatible vertical scale of internal waves and turbulence during a shear-instability event is revealed in Fig. 14.

b. Comparison with modified GM spectrum

Away from obvious sources and sinks of internal waves, observed oceanic velocity spectra in the internal wave frequency band often agree well with the GM-79 internal wave spectral model (Garrett and Munk 1975). At the equator, however, the GM-79 spectrum degenerates. Levine (2002, hereafter LE) proposes a modified GM spectrum aimed at removing inconsistencies and ambiguities in the existing version. Levine's model spectrum removes the singularity at the equator. This revised model spectrum changes its spectral slope at the semidiurnal frequency, $\omega_{S2} = 1.45 \times 10^{-4} \text{ s}^{-1}$. At frequencies greater than ω_{S2} , the vertical velocity spectrum at the equator in Levine's model has a form as

$$\begin{aligned} \Phi_w^L &= E_{\text{ref}} \omega_{S2} N [N^2 (N_{\text{ref}} - \omega_{S2})]^{-1} \\ &\approx E_{\text{ref}} N_{\text{ref}}^{-1} \omega_{S2} N^{-1}, \end{aligned} \quad (5)$$

where N_{ref} is the arbitrary reference buoyancy frequency, and E_{ref} is the reference dimensional energy. The approximate form is valid in the upper ocean where the buoyancy frequency is at least an order of magnitude greater than the semidiurnal tidal frequency. The E_{ref} is not prescribed in the model and depends on the N_{ref} . Levine estimates E_{ref} to be about $2 \times 10^{-3} \text{ m}^2 \text{ s}^{-2}$ given $N_{\text{ref}} = 0.0052 \text{ s}^{-1}$ (3 cph) on the basis of horizontal velocity spectra computed from the TAO mooring measurements at the equator.

Our observed Lagrangian and Eulerian vertical velocity spectra are white at frequencies much below the near- N spectral peak in the internal wave frequency band and have a spectral level about $2 \times 10^{-3} \text{ m}^2 \text{ s}^{-1}$. For N of 0.015 s^{-1} , our estimate of E_{ref} is $1.1 \times 10^{-3} \text{ m}^2 \text{ s}^{-2}$, about half of Levine's result.

c. Relationship between waves and turbulence

[Gregg et al. \(1985\)](#) suggest that internal waves in the deep-cycle layer are generated at the base of the convective mixed layer. These waves trigger the shear instability which then produces the observed strong turbulence. [Wijesekera et al. \(1991\)](#) propose two mechanisms generating internal waves at the base of the convective mixed layer. In Gregg's hypothesis, remotely generated internal waves are needed for generating the deep-cycle turbulence.

[Clayson and Kantha \(1999\)](#) suggest that the deep-cycle turbulence is a result of nighttime enhancement of the mean shear and that the observed increasing internal wave activity is simply part of the shear instability. Using the LES model, Wang and Müller (2001) appropriately resolve both the turbulence and internal waves. They conclude the local shear instability results in the intensified internal waves and turbulence in the deep-cycle layer. Based on the linear stability analysis, [Mack and Hebert \(1997\)](#) and [Sun et al. \(1998\)](#) successfully explain observed internal waves in the deep-cycle layer as a result of shear instability. These studies suggest that remotely generated internal waves are not needed for generating deep-cycle turbulence, although they are the products of the shear instability.

Our observations support the hypothesis suggested by [Mack and Hebert \(1997\)](#), [Sun et al. \(1998\)](#), and [Clayson and Kantha \(1999\)](#) that internal waves are generated in the deep-cycle layer by the shear instability. Some waves break and supply energy to the turbulence, and some other waves radiate away forming the unique background near- N waves ([Fig. 13](#)). These escaped internal waves are long-lived and uncorrelated with the deep-cycle turbulence. During the shear instability, locally generated internal waves dominate and correlate with turbulence mixing. These near- N waves may also act to trigger the shear instability, but our observations provide no direct evidence.

d. Heat budget and termination of El Niño

In the deep-cycle layer, the average heat flux estimated by float measurements is $O(100\text{s}) \text{ W m}^{-2}$ in the first three days during which the reduced shear squared is positive, that is, $\text{Ri} < 1/4$, and strong. This estimated heat flux roughly balances with the net heat flux at the sea surface ([Wang and McPhaden 2001](#)). These are the two primary heat flux components in the central equatorial Pacific.

[Wang and McPhaden \(2001\)](#) and [Vialard et al. \(2001\)](#) conclude that the rapid cooling of the sea surface temperature at the central equatorial Pacific during the transition from El Niño to La Niña in May–June 1998 was due to an abnormally strong turbulence mixing across the base of the mixed layer. Wang and McPhaden estimate the advective and time rate change terms in the heat balance equation integrated over the surface mixed layer and regard the residual as the turbulence heat flux across the base of the mixed layer. In June of 1998, they found the residual cooling of 2° to $5^\circ\text{C month}^{-1}$ in an $\sim 15 \text{ m}$ surface mixed layer, corresponding to a turbulent heat flux of $46.5\text{--}115 \text{ W m}^{-2}$ across the bottom of the surface mixed layer.

The deep-cycle turbulence could potentially drain a significant amount of heat across the base of the surface mixed layer. An extra turbulence heat loss of 100 W m^{-2} from the surface mixed layer could reduce a 10-m surface mixed layer temperature by nearly 7°C in a month, as found in May–June of 1998. During that period the EUC moved closer to the surface. The reduced shear squared ($S^2 - 4N^2$) computed from TAO mooring measurements was strong and positive during May and June of 1998 (not shown). The shoaling of the EUC, combined with the energetic deep-cycle turbulence suggested by the positive reduced shear squared, provide ideal circumstance for mixing the cold EUC water with the abnormally warm water in the surface mixed layer. The turbulence heat flux in the deep-cycle layer must have played a crucial dynamic role in terminating the 1998 El Niño.

7. Summary

Measurements of a Lagrangian float deployed in the deep-cycle layer at the central equatorial Pacific revealed significant nighttime enhancements of ϵ , χ , and the vertical velocity variance σ_w^2 . Dissipation ϵ was estimated from the Lagrangian frequency spectrum of the vertical acceleration $\Phi_{d_t w}$, and χ from the Lagrangian frequency spectrum of the thermal change rate $\Phi_{d_t \theta}$. In the turbulence inertial subrange, $\Phi_{d_t w}$ and $\Phi_{d_t \theta}$ are white and their spectral levels are proportional to ϵ and χ , respectively (Tennekes and Lumley 1972; Yeung 2001). Both ϵ and χ decreased by a factor of 20 in 4 days. The eddy diffusivity estimated using ϵ (Osborn 1980) agreed well with the thermal diffusivity estimated using χ (Osborn and Cox 1972), as found in previous microstructure measurements (Peters et al. 1988). This agreement confirms the scaling of $\Phi_{d_t w}$ and $\Phi_{d_t \theta}$ in the inertial subrange.

For linear internal waves, the GM79 (Garrett and Munk 1975) spectrum of vertical velocity is white at frequencies much smaller than N . For vertically varying N , a spectral peak may exist at a frequency slightly below the local N as a result of “turning-point effect” (Desaubies 1973). Observed Lagrangian frequency spectra of vertical velocity are white at low frequencies and have a peak slightly below N . Nevertheless, the observed near- N spectral peak often exceeds the background by nearly one decade. These near- N internal waves are likely not a result of turning point effect, but rather a special species existing in the low-Ri shear stratified layer.

Linear stability analyses have suggested that the previously observed enhanced internal wave activity could be explained by the shear instability of the EUC, consistent with results of various numerical models from a simple 1D model to some complex LES models. These models suggest that observed near- N internal waves are results of the shear instability, rather than the cause. Our observed enhanced internal wave activity repeated diurnally, even during the day when the deep-cycle turbulence was weak, presumably in absence of the shear instability. These energetic internal waves during the period of weak turbulence could either have been generated via other mechanisms, for example, from the base of the surface mixed layer, or generated via shear instability at remote locations propagating through the observation site. The propagation nature of internal waves and their small horizontal and temporal scales make it difficult to distinguish these mechanisms through observations.

Vertical velocity spectra computed from Eulerian measurements agreed with those computed from Lagrangian measurements at frequencies below N implying that the linear internal wave dynamics were appropriate in this frequency range. During the first three days, the Lagrangian float flowed in a depth range of near-zero zonal velocity; there was no Doppler shift of frequency between the Lagrangian and Eulerian spectra. On the fourth day, the float flowed in a depth range of the mean zonal current between -0.3 and -0.1 m s⁻¹ and a Doppler shift frequency of near- N internal waves was identified. These waves appeared to have a zonal wavelength of 360 m, vertical wavelength of 120 m, westward phase speed of 0.5 m s⁻¹, and vertical phase speed of 0.27 m s⁻¹. These estimates are consistent with previous observations (Sun et al. 1998; Mack and Hebert 1997).

An event of shear instability was identified from the wavelet analysis of vertical velocity variance recorded by the Lagrangian float. The vertical velocity variance in the near- N frequency band grew exponentially with a timescale of ~ 1 h, followed by an increase of vertical velocity variance in the turbulence inertial subrange with an exponential timescale of ~ 10 min. The ϵ during the event was $\sim 2 \times 10^{-5}$ W kg⁻¹ and χ was $\sim 10^{-4}$ °C² s⁻¹. An extremely large turbulence heat flux of ~ 4000 W m⁻² during the event was inferred.

This analysis demonstrates that the Lagrangian float accurately captures properties of internal waves and turbulence in an energetic turbulent flow. The comparison between Eulerian and Lagrangian frequency spectra provides valuable information of properties of internal waves. Combining Eulerian measurements taken from the TAO mooring and the remote transmission of float data, it is possible to monitor the turbulence mixing in the equatorial Pacific. Although the reduced shear squared is a good indicator for the deep-cycle turbulence, a more physics-based parameterization scheme that will provide proper scaling for the deep-cycle turbulent fluxes is needed.

Acknowledgments

We are grateful to the crew of the *Ka'imimoana* for helping us deploy the Lagrangian floats. We would like to thank June Firing at the University of Hawaii who provided processed shipboard ADCP data. Paul Freitag, Dai McClurg, and Linda Stratton of NOAA/PMEL provided processed velocity, temperature, and meteorological data from TAO moorings, and Greg Johnson of PMEL provided historical CTD data, which were crucial to this analysis. Discussions with Weiming Wang of NOAA/PMEL about the heat budget in the equatorial surface mixed layer and with Dailin Wang at University of Hawaii about the LES model of the deep-cycle turbulence were very useful. This analysis was supported by the National Science Foundation under Grant OCE9906632 (Ren-Chieh Lien and Eric D'Asaro) and by NOAA's Office of Oceanic and Atmospheric Research (Michael McPhaden).

REFERENCES

- Bell T. H., 1978: Radiation damping of inertial oscillations in the upper ocean. *J. Fluid Mech.*, **88**, 289–308. [Find this article online](#)
- Caldwell D. R., R.-C. Lien, J. N. Moum, and M. C. Gregg, 1997: Turbulence decay and restratification in the equatorial ocean surface layer following nighttime convection. *J. Phys. Oceanogr.*, **27**, 1120–1132. [Find this article online](#)
- Clayson C. A., and L. H. Kantha, 1999: Turbulent kinetic energy and its dissipation rate in the equatorial mixed layer. *J. Phys. Oceanogr.*, **29**, 2146–2166. [Find this article online](#)
- Crawford W. R., and T. R. Osborn, 1981: Control of equatorial ocean currents by turbulent dissipation. *Science*, **212**, 539–540. [Find this article online](#)
- D'Asaro E. A., and G. T. Dairiki, 1997: Turbulence intensity measurements in a wind driven mixed layer. *J. Phys. Oceanogr.*, **27**, 2009–2022. [Find this article online](#)
- D'Asaro E. A., and R.-C. Lien, 2000: Lagrangian measurements of waves and turbulence in stratified flows. *J. Phys. Oceanogr.*, **30**, 641–655. [Find this article online](#)
- D'Asaro E. A., D. M. Farmer, J. T. Osse, and G. T. Dairiki, 1996: A Lagrangian float. *J. Atmos. Oceanic Technol.*, **13**, 1230–1246. [Find this article online](#)
- Desaubies Y. J. F., 1973: Internal waves near the turning point. *Geophys. Fluid Dyn.*, **5**, 143–154. [Find this article online](#)
- Dillon T. M., and D. R. Caldwell, 1980: The Batchelor spectrum and dissipation in the upper ocean. *J. Geophys. Res.*, **85**, 1910–1916. [Find this article online](#)
- Dillon T. M., J. N. Moum, T. K. Chereskin, and D. R. Caldwell, 1989: Zonal momentum balance at the equator. *J. Phys. Oceanogr.*, **19**, 561–570. [Find this article online](#)
- Farmer D. M., E. A. D'Asaro, M. V. Trevorrow, and G. T. Dairiki, 1997: Three-dimensional structure in a tidal convergence front. *Cont. Shelf Res.*, **15**, 1649–1673. [Find this article online](#)
- Fung J. C. H., J. C. R. Hunt, N. A. Malik, and R. J. Perkins, 1992: Kinematic simulation of homogeneous turbulence by unsteady random Fourier modes. *J. Fluid Mech.*, **236**, 281–318. [Find this article online](#)
- Garrett C. J. R., and W. H. Munk, 1975: Space–time scales of internal waves: A progress report. *Annu. Rev. Fluid Mech.*, **11**, 339–369. [Find this article online](#)
- Gregg M. C., H. Peters, J. C. Wesson, N. S. Oakey, and T. J. Shay, 1985: Intensive measurements of turbulence and shear in the equatorial undercurrent. *Nature*, **318**, 140–144. [Find this article online](#)
- Hebert D., J. N. Moum, C. A. Paulson, and D. R. Caldwell, 1992: Turbulence and internal waves at the equator. Part II: Details of a single event. *J. Phys. Oceanogr.*, **22**, 1346–1356. [Find this article online](#)
- Levine M. D., 2002: A modification of the Garrett–Munk internal wave spectrum. *J. Phys. Oceanogr.*, in press.
- Lien R.-C., D. R. Caldwell, M. C. Gregg, and J. N. Moum, 1995: Turbulence variability at the equator in the central Pacific at the beginning of the 1991–93 El Niño. *J. Geophys. Res.*, **100**, 6881–6898. [Find this article online](#)
- Lien R.-C., M. J. McPhaden, and M. C. Gregg, 1996: High-frequency internal waves in the upper central equatorial Pacific and their possible relationship to deep-cycle turbulence. *J. Phys. Oceanogr.*, **26**, 581–600. [Find this article online](#)
- Lien R.-C., E. A. D'Asaro, and G. Dairiki, 1998: Lagrangian frequency spectra of vertical velocity and vorticity in high-Reynolds-number oceanic turbulence. *J. Fluid Mech.*, **362**, 177–198. [Find this article online](#)
- Mack A. P., and D. Hebert, 1997: Internal gravity waves in the upper eastern equatorial Pacific: Observations and numerical solutions. *J. Geophys. Res.*, **102**, 21081–21100. [Find this article online](#)
- McCreary J. P., 1981: A linear, stratified ocean model of the equatorial undercurrent. *J. Philos. Trans. Roy. Soc. London, Ser. A.*, **298**, 603–635. [Find this article online](#)
- McPhaden M. J., 1999: Genesis and evolution of the 1997–98 El Niño. *Science*, **283**, 950–954. [Find this article online](#)
- McPhaden M. J., and H. Peters, 1992: Diurnal cycle of internal wave variability in the equatorial Pacific Ocean: Results from moored

observations. *J. Phys. Oceanogr.*, **22**, 1317–1329. [Find this article online](#)

McPhaden M. J., Coauthors, 1998: The Tropical Ocean–Global Atmosphere (TOGA) observing system: A decade of progress. *J. Geophys. Res.*, **103**, 14169–14240. [Find this article online](#)

Moum J. N., D. R. Caldwell, and C. A. Paulson, 1989: Mixing in the equatorial surface layer and thermocline. *J. Geophys. Res.*, **94**, 2005–2021. [Find this article online](#)

Moum J. N., D. Hebert, C. A. Paulson, and D. R. Caldwell, 1992: Turbulence and internal waves at the equator. Part I: Statistics from towed thermistors and a microstructure profiler. *J. Phys. Oceanogr.*, **22**, 1330–1345. [Find this article online](#)

Müller P., D. J. Olbers, and J. Willebrand, 1978: The IWEX spectrum. *J. Geophys. Res.*, **83**, 479–500. [Find this article online](#)

Osborn T. R., 1980: Estimates of the local rate of vertical diffusion from dissipation measurements. *J. Phys. Oceanogr.*, **10**, 83–89. [Find this article online](#)

Osborn T. R., and C. S. Cox, 1972: Oceanic fine structure. *Geophys. Fluid Dyn.*, **3**, 321–345. [Find this article online](#)

Percival D. B., and P. Guttorp, 1994: Long-memory processes, the Allan variance and wavelets. *Wavelets in Geophysics*, E. Foufoula-Georgiou and P. Kumar, Eds., Academic Press, 325–344.

Peters H., M. C. Gregg, and J. M. Toole, 1988: On the parameterization of equatorial turbulence. *J. Geophys. Res.*, **93**, 1199–1218. [Find this article online](#)

Peters H., 1989: Meridional variability of turbulence through the equatorial undercurrent. *J. Geophys. Res.*, **94**, 18003–18009. [Find this article online](#)

Peters H., and T. B. Sanford, 1994: The diurnal cycle of the upper equatorial ocean: Turbulence, fine-scale shear, and mean shear. *J. Geophys. Res.*, **99**, 7707–7723. [Find this article online](#)

Philander S. G. H., and R. C. Pacanowski, 1980: The generation of Equatorial Currents. *J. Geophys. Res.*, **85**, 1123–1136. [Find this article online](#)

Skyllingstad E. D., and D. W. Denbo, 1994: The role of internal gravity waves in the equatorial current system. *J. Phys. Oceanogr.*, **24**, 2093–2110. [Find this article online](#)

Sun C., W. D. Smyth, and J. N. Moum, 1998: Dynamic instability of stratified shear flow in the upper equatorial Pacific. *J. Geophys. Res.*, **103**, 10323–10337. [Find this article online](#)

Tennekes H., and J. L. Lumley, 1972: *A First Course in Turbulence*. The MIT Press, 300 pp.

Vialard J., C. Menkes, J.-P. Boulanger, P. Delecluse, E. Guilyardi, M. J. McPhaden, and G. Madec, 2001: A model study of oceanic mechanisms affecting equatorial Pacific sea surface temperature during the 1997–98 El Niño. *J. Phys. Oceanogr.*, **31**, 1649–1675. [Find this article online](#)

Wang D., and P. Müller, 2002: Effects of equatorial undercurrent shear on upper-ocean mixing and internal waves. *J. Phys. Oceanogr.*, **32**, 1041–1057. [Find this article online](#)

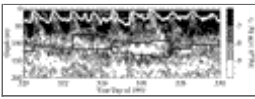
Wang D., J. C. McWilliams, and W. G. Large, 1998: Large-eddy simulation of the diurnal cycle of deep equatorial turbulence. *J. Phys. Oceanogr.*, **28**, 129–148. [Find this article online](#)

Wang W., and M. J. McPhaden, 2001: Surface layer temperature balance in the equatorial Pacific during the 1997–98 El Niño and 1998–99 La Niña. *J. Climate*, **14**, 3393–3407. [Find this article online](#)

Wijesekera H. W., and T. M. Dillon, 1991: Internal waves and mixing in the upper equatorial Pacific Ocean. *J. Geophys. Res.*, **96**, 711–7125. [Find this article online](#)

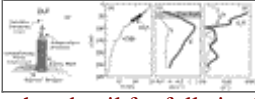
Williams R. M., and C. A. Paulson, 1977: Microscale temperature and velocity spectra in the atmospheric boundary layer. *J. Fluid Mech.*, **82**, 547–567. [Find this article online](#)

Yeung P. K., 2001: Lagrangian characteristics of turbulence and scalar transport in direct numerical simulations. *J. Fluid Mech.*, **427**, 241–274. [Find this article online](#)



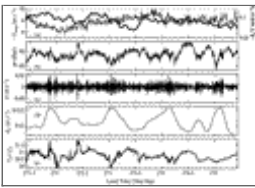
[Click on thumbnail for full-sized image.](#)

FIG. 1. Contours of $\log_{10}\epsilon$ observed at equator 140°W during the TIWE. The thick white curve shows the base of the surface mixed layer. Two thin white curves delineate the depth range where $Ri < 1/2$. The black stair shows the depth of the EUC speed maximum (in some cases there were two local maxima). At nighttime, strong turbulence mixing, $\epsilon > 10^{-7} \text{ W kg}^{-1}$, penetrated 20–40 m below the surface mixed layer, called the deep-cycle layer, where the Ri is low



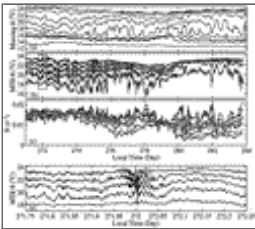
[Click on thumbnail for full-sized image.](#)

FIG. 2. (a) Deep Lagrangian Float. The hull of the DLF is about 0.7 m long and the drogue opens up to about 1 m in diameter. (b) The thin curve is the background temperature profile taken from CTD immediately before the deployment of the DLF and the squares are temperature measured by the DLF. (c) The velocity profiles were taken from the shipboard ADCP on board the *Ka'imimoana*. The horizontal gray bar indicates the depth range of the DLF during the experiment. (d) The stratification N (thin curve) and the vertical shear of the zonal current (thick curve) were computed from the CTD and ADCP



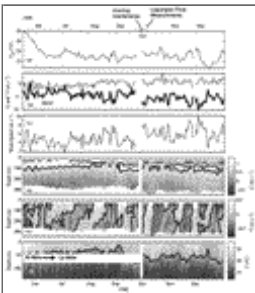
[Click on thumbnail for full-sized image.](#)

FIG. 3. Time series of (a) easterly wind speed (thin curve) and the vertical shear of zonal velocity across the base of the surface mixed layer (thick curve) computed from hourly averaged current meter measurements at 10- and 25-m depths, (b) pressure measured by the DLF, (c) vertical velocity of the DLF, (d) 4-h lowpass-filtered rms vertical velocity, and (e) temperature fluctuations observed by the DLF during the 4-day high-sampling-rate period of the float experiment.



[Click on thumbnail for full-sized image.](#)

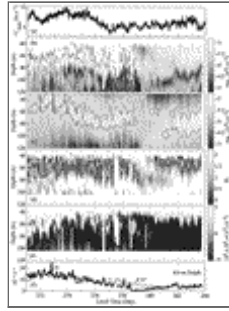
FIG. 4. Moored time series of temperature measurements at 0° , 140°W taken by (a) standard temperature sensors sampling at 10-min intervals from depths of 5, 10, 25, 45, 60, 80, 100, 120, 140, and 200 m, and by (b) MTRs sampling at 20-s intervals from depths of 25, 35, 45, 55, and 70 m during the float experiment. (c) Time series of buoyancy frequency computed using combined hourly lowpass-filtered temperature measurements of MTR and standard temperature sensors assuming a constant salinity of 35 psu at 25, 35, 45, 55, 60, 70, and 80 m, and (d) a short segment of high-resolution MTR measurements. The box in (b) marks the time segment shown in (d). (b) MTR measurements were plotted every other 50 data points, i.e., 1000-s time interval. (d) The full resolution, 20-s sampling interval, of temperature fluctuations. The gray thick curve in (c) represents the average buoyancy frequency between depths 25 and 80 m



[Click on thumbnail for full-sized image.](#)

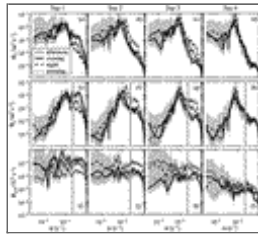
FIG. 5. Background conditions at equator, 140°W in 1998: (a) air temperature, (b) x component (thick curve) and y component (thin curve) of surface wind velocity, (c) surface wind speed, (d) contour of zonal velocity U , (e) contour of meridional velocity V ,

and (f) contour of temperature T . Thick solid curves in (d), (e), and (f) represent contour lines of $U = 1 \text{ m s}^{-1}$, $V = 0 \text{ m s}^{-1}$, and $T = 20^\circ\text{C}$, respectively. Periods of the mooring maintenance and the float experiment are marked on top of the time axis. Velocity measurements taken by the mooring-mounted ADCP are used for generating contours in (d) and (e). Temperature measurements taken by standard thermistors mounted on the mooring are used to generate the contour plot in (f)



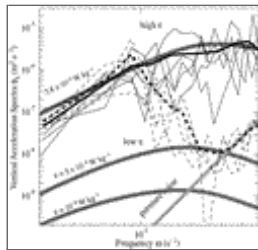
Click on thumbnail for full-sized image.

FIG. 6. Background conditions at equator, 140°W in 1998 during the deployment of MTRs encompassing the period of float experiment; (a) magnitude of zonal surface wind, (b) shear squared, (c) N squared, (d) Richardson number, (e) reduced shear squared, and (f) shear squared (thick curve) and four N squared (thin curve) at 45-m depth. Yearday 271 corresponds to 29 Sep. Black curves in (c) and (d) represent contour lines of $S^2 = 10^{-3} \text{ s}^{-2}$ and $N^2 = 10^{-3.5} \text{ s}^{-2}$, respectively. White curves in (d) and (e) represent contour lines of $\text{Ri} = 1/4$ and $S^2 = 4N^2$, respectively



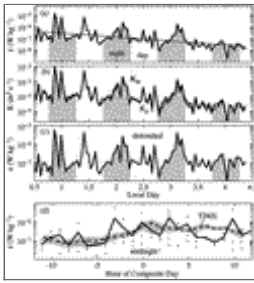
Click on thumbnail for full-sized image.

FIG. 7. Lagrangian frequency spectra of vertical velocity $\Phi_w(\omega)$, vertical acceleration $\Phi_a(\omega)$, and the time rate change of temperature $\Phi_{dT}(\omega)$. Spectra were computed in 6-h bins dividing each day into four time periods: 1200–1800 LT (afternoon, thin curves), 1800–2400 LT (evening, thick solid curves), 2400–0600 LT (night, thick dashed curves), and 0600–1200 LT (morning, thick dotted curves). The vertical gray lines indicate frequencies of 0.02 s^{-1} , slightly above the buoyancy frequency



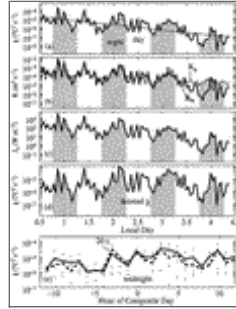
Click on thumbnail for full-sized image.

FIG. 8. Lagrangian frequency spectra of vertical acceleration during periods of $\epsilon > 10^{-6} \text{ W kg}^{-1}$ (thin solid curves) and periods of $\epsilon < 10^{-7} \text{ W kg}^{-1}$ (thin dashed curves). The thick solid and thick dashed curves represent their means. The thick gray curve showing ω^4 spectral slope represents the effect of the pressure noise. The other three gray curves represent vertical acceleration spectra of isotropic turbulence (Lien et al. 1998) assuming the large eddy frequency being 0.01 s^{-1} for ϵ of $3.8 \times 10^{-6} \text{ W kg}^{-1}$, $5 \times 10^{-8} \text{ W kg}^{-1}$, and $10^{-8} \text{ W kg}^{-1}$



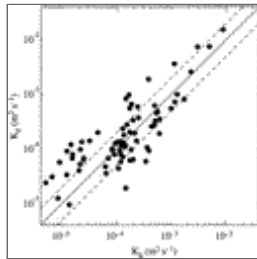
Click on thumbnail for full-sized image.

FIG. 9. Time series of (a) ϵ estimated from Lagrangian vertical acceleration frequency spectra; (b) the eddy viscosity (thick curve), $K_m = \epsilon / [(d_z u)^2 + (d_z v)^2]^{-1}$, and the eddy diffusivity (thin curve), $K_\rho = 0.2\epsilon N^{-2}$; (c) the detrended ϵ ; and (d) the composite day of the detrended ϵ (thick curve). Dots in (d) are individual values of detrended ϵ . The thin curve in (a) shows the linear trend of $\log_{10}(\epsilon)$. The thick dashed curve in (d) shows ϵ in a composite day of microstructure measurements taken in TIWE 1991 (Lien et al. 1995)



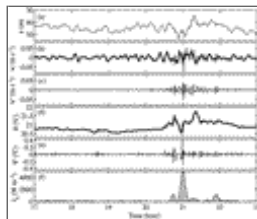
Click on thumbnail for full-sized image.

FIG. 10. Time series of (a) χ estimated from Lagrangian frequency spectra of thermal change rate; (b) the thermal diffusivity, $K_h = 0.5\chi(d_z \bar{\theta})^{-2}$, and the eddy diffusivity, $K_\rho = 0.2\epsilon N^{-2}$; (c) the turbulence heat flux $J_q = \rho C_p K_h d_z \bar{\theta}$; (d) the detrended χ ; and (e) the composite day of the detrended χ (thick solid curve). Dots in (e) are individual values of detrended χ . The thin curve in (a) shows the linear trend of $\log_{10}(\chi)$. The thick dashed curve in (e) shows $20 \times \epsilon$ (Fig. 9), which exhibits a clear correlation with χ



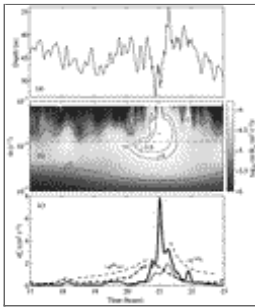
Click on thumbnail for full-sized image.

FIG. 11. Scatterplots of K_ρ computed using estimates of ϵ (Osborn 1980) and K_h computed using estimates of χ (Osborn and Cox 1972). The solid line indicates $K_\rho = K_h$, and the two dashed lines indicate a ratio of 2 and 0.5



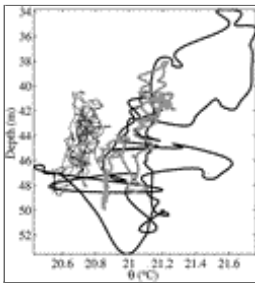
Click on thumbnail for full-sized image.

FIG. 12. Time series from 29 Sep 1998 of (a) float depth, (b) vertical velocity, (c) perturbation vertical velocity, (d) temperature, (e) perturbation temperature, and (f) heat flux. The thick curves in (b) and (d) indicate the low-pass vertical velocity and temperature, respectively, at timescale greater than 10 min



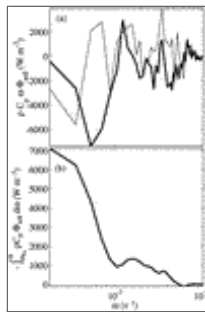
[Click on thumbnail for full-sized image.](#)

FIG. 13. Time series in 29 Sep of (a) float depth, (b) vertical velocity variance in the time–frequency domain computed from the wavelet analysis, and (c) vertical velocity variance at frequency between 0.0065 and 0.0131 s^{-1} (thick dashed curve), between 0.0131 and 0.0262 s^{-1} (thin solid curve), between 0.0131 and 0.0524 s^{-1} (gray curve), and between 0.0131 and 0.1047 s^{-1} (thick solid curve). The thin dashed curves represent the exponential growing rate and decaying rate of vertical velocity variance of internal waves and turbulence. The horizontal dashed line in (b) indicates the buoyancy frequency



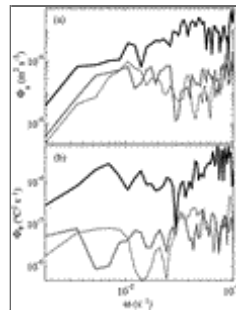
[Click on thumbnail for full-sized image.](#)

FIG. 14. Temperature–depth plot. The thin curve is between 1700 and 2030 LT 29 Sep. The thick solid curve is during the turbulent event between 2030 and 2200 LT and the gray curve is after 2200 LT.



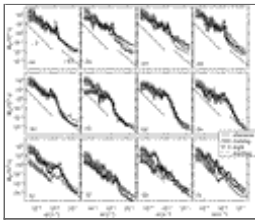
[Click on thumbnail for full-sized image.](#)

FIG. 15. (a) Variance preserving plots of cospectrum (thick curve) and quadspectrum (thin curve) between temperature and vertical velocity, and (b) the heat flux computed by integrating the cospectrum from the Nyquist frequency toward lower frequency



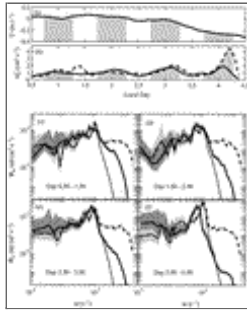
[Click on thumbnail for full-sized image.](#)

FIG. 16. (a) Spectra of vertical acceleration and (b) spectra of the time rate of change of temperature. Thin curves are spectra computed between 1800 and 1900 LT, thick curves between 2030 and 2130 LT, and the gray curves between 2200 and 2300 LT



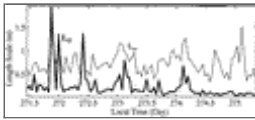
[Click on thumbnail for full-sized image.](#)

FIG. 17. Temperature spectra of MTR measurements in the first 12 days. Spectra are computed in 6-h segments. These are averages of spectra computed from measurements taken at 25, 35, 45, and 55-m depth. Symbols are as described in [Fig. 7](#). Spectral slopes of -2 and $-5/3$ are shown for reference



[Click on thumbnail for full-sized image.](#)

FIG. 18. Comparison of Lagrangian and Eulerian observations: (a) time series of mean zonal velocity averaged between depth 35 and 55 m, (b) time series of vertical velocity variances of low-pass filtered measurements of Lagrangian floats (solid curve) and MTR sensors at 45 m (dashed curve), and (c–f) vertical velocity spectra computed from measurements of the Lagrangian float (thick solid curves) and of the MTR sensor at 45-m depth (thick dashed curves). The thin curves in (c–f) represent the spectra of low-pass filtered MTR measurements used for computing the vertical velocity variance in (b)



[Click on thumbnail for full-sized image.](#)

FIG. 19. Time series of Ozmidov scale L_O (thick solid curve), and internal wave vertical displacement scale L_w (thin solid curve)

Corresponding author address: Dr. Ren-Chieh Lien, Applied Physics Laboratory and School of Oceanography, University of Washington, 1013 NE 40th Street, Seattle, WA 98105. E-mail: lien@apl.washington.edu

[top](#) ▲



© 2008 American Meteorological Society [Privacy Policy and Disclaimer](#)
 Headquarters: 45 Beacon Street Boston, MA 02108-3693
 DC Office: 1120 G Street, NW, Suite 800 Washington DC, 20005-3826
amsinfo@ametsoc.org Phone: 617-227-2425 Fax: 617-742-8718
 Allen Press, Inc. assists in the online publication of AMS journals.